Front. Earth Sci. 2022, 16(2): 221–235
https://doi.org/10.1007/s11707-020-0863-8

RESEARCH ARTICLE

The scattering mechanism of squall lines with C-Band dual polarization radar. Part I: echo characteristics and particles phase recognition

Jiashan ZHU[1], Ming WEI (✉)[1], Sinan GAO[1], Hanfeng HU[1], Lei MA[2]

1 Collaborative Innovation Center on Forecast and Evaluation of Meteorological Disasters, Nanjing University of Information Science & Technology, Nanjing 210044, China
2 Leihua Electronic Technology Research Institute of Aviation Industry Corporation of China, Wuxi 214063, China

© Higher Education Press 2021

Abstract Squall line is a kind of common mesoscale disaster weather. At present, there are few studies on the elaborate detection of squall line by dual polarization radar. With the dual polarization upgrade of weather radar network, we need to study the relationship between squall line echoes of base data and polarization data to reveal new echo phenomena and formation mechanisms. The relationship between radar parameters and atmospheric physical processes also need to be examined. Based on the NUIST CDP radar, a squall line in the Yangtze and Huaihe River basin that occurred from July 30 to 31, 2014 is analyzed. The results show that polarization parameters have obvious advantages in the characteristics analysis of size, phase state, shape and orientation of the water condensate particles. The phase states of water condensate particles in convection cell can be distinguished through comparative discussion. Several phase states exist in the squall line, including small, medium and large raindrops, melting hails, dry hails and ice crystal particles and the Z_{DR} column can be used to identify the location of the main updraft. In addition, the polarization parameters are more sensitive to the melting layer. The gust front is presented as a narrow linear echo in Z affected by strong turbulence. It is an obvious velocity convergence line in V and approximately 0.70 in ρ_{HV}. The Z_{DR} can be used as a criterion to distinguish the horizontal and vertical scale of turbulence. The deforming turbulence, which is affected by environmental airflow, will cause an abnormally high Z_{DR} in the gust front and a negative Z_{DR} before and after the gust front. The variation of Z_{DR} depends on the turbulence arrangement, orientation and relative position between turbulence and radar. These dual polarization parameter characteristics offer insights into understanding the structure and evolution of the squall line.

Keywords dual polarization Doppler radar, RHI, squall line, gust front, turbulence

Received August 18, 2020; accepted December 13, 2020

E-mail: wm_nuist@126.com

1 Introduction

Weather radar is an important tool for disaster weather monitoring and early warnings. Recently, China upgraded its new generation of Doppler weather radar networks to a dual polarization Doppler weather radar network. Although lots of studies on weather radar exist, our understanding about several questions is far from complete, including the theory of electromagnetic scattering, signal analysis, data quality control, convective echo analysis and quantitative precipitation estimation.

In convective echo analysis, the squall line is a strong convective cloud belt formed by many thunderstorm cells (including some supercells) that are arranged laterally. Geerts (1998) used high-resolution radar data to define criteria for identifying squall lines. According to the relative position of stratiform area and convective area, squall lines are divided into trailing stratiform, leading stratiform and parallel stratiform (Parker and Johnson, 2000). Cases of tracking stratiform occupy approximately 60% of all types of squall lines. Gallus et al. (2008) summarized nine kinds of mesoscale linear convection systems after a long period of data collection, analysis and statistics, including isolated cells, clusters of cells, broken lines, no stratiform, tailing stratiform, parallel stratiform, leading stratiform, bow echo and nonlinear systems. In the study of the internal structure of the squall line, Houze et al. (1989) observed that there is a gust front, low pressure in

front of the squall line, thunderstorm high pressure in the squall line, wake low pressure, cold pool, stratiform precipitation and other characteristics in the back of the squall line, and considered the development of an updraft in front of the squall line as the key to the development of the squall line system. Meng et al. (2013) explored the general characteristics of squall lines in East China and found that the highest frequency of squall lines occurred at the intersection of Shandong, Henan, Anhui and Jiangsu. In addition, Hebei, Guangdong and Fujian experienced the second highest frequencies. The occurrence of the squall line had significant seasonal variations. The squall line reached its peak frequency in July, and its seasonal movement may be related to the seasonal displacement of the baroclinic zone between the subtropics and tropics.

The organizational form, internal structure, maintenance mechanism and occurrence probability of squall line have been studied maturely. However, China's dual polarization radar network is under construction. There are only a few number of well-functioning polarization radars. Most studies of mesoscale convective weather based on dual polarization radar are about the supercells (Bluestein et al., 2007; Pan et al., 2020; Romine et al., 2008). Studies about the size, phase state, shape and orientation of water condensate particles in squall lines are still far from complete. Besides, all operational weather radars in the network use precipitation patterns (volume coverage patterns) VCP11 and VCP21, which are stipulated by the China Meteorological Administration (CMA) (available at CMA website), and provided the data about weather information of all directions, large ranges and multiple elevation levels. However, in the severe convective weather process which can easily cause major disasters, the vertical structure plays a more important role than the horizontal structure. So it is great significant to obtain accurate range height indicator (RHI) scan pattern data.

In this study, a squall line process that occurred in the Yangtze and Huaihe River basin on July 30, 2014 was analyzed by using radar base data collected by the C-Band Dual Polarization Full Coherent Pulse Doppler Weather Radar at Nanjing University of Information Science & Technology (NUIST CDP radar), NCEP-NCAR reanalysis data and conventional meteorological observation data. To fill the study gap, the purpose of this paper is to examine the relationship between the base data and polarization data of squall line echoes, reveal the new echo phenomenon and formation mechanism, and understand the relationship between radar parameters and atmospheric physical processes.

2 Data sets and methods

2.1 Radar data

There was a squall line in the Yangtze and Huaihe River basin from July 30 to 31, 2014, which severely affected Henan, Anhui and Jiangsu. It formed at 18:00, July 30 (Beijing time, the same below), moved from north-west to south-east, gradually weakened and eventually dissipated after passing over Nanjing at 05:00 on the 31st. Affected by the squall line, some areas in Jiangsu had strong convective weather processes, such as thunderstorms, gales and short-term heavy rainfall. This squall line is also recorded by the NUIST CDP radar. The main characteristics of this radar are listed in Table 1. In this study, the pulse width, radial resolution, pulse repetition frequency (PRF) and observation range of NUIST CDP radar is 0.5 μs, 75 m, 1000 Hz and 150 km, respectively.

Table 1 Main characteristics of NUIST CDP radar

Item	Characteristics
Wavelength/cm	5.45
Beam Width/(°)	0.54
Pulse Width/μs	0.3, 0.5, 1.0, 2.0
Radial resolution/m	45, 75, 150, 300
Pulse Repetition Frequency/Hz	300–2000
Maximum unambiguous distance/km	75–500
Maximum unambiguous speed/(m·s^{-1})	4–27
Peak Power/kW	⩾250
Polarization	Linear: horizontal and vertical
Antenna Gain/dB	48.5 for horizontal channel 48.6 for vertical channel
Signal Processor	RVP900 and WRSP
Minimal Detectable Signal/dBm	⩽−109 for 0.5 μs pulse width ⩽−112 for 2.0 μs pulse width
Resolution	1 dB for reflectivity (Z) 1 m/s for Doppler radial velocity (V) 1 m/s for Doppler spectral width (W) 0.2 dB for differential reflectivity (Z_{DR}) 2 ° for differential propagation phase shift (Φ_{DP}) 0.01 for correlation coefficient (ρ_{HV})

The VCP stipulated by CMA is adopted in operational radar observations, and only plan position indicator (PPI) scan pattern is carried out. Echoes in PPI are directly observed. However, echoes in RHI is usually obtained by patchwork or interpolation. The authenticity and resolution of patchwork RHI data are obviously poorer than that of direct RHI scan pattern (Langston et al., 2007). Besides, in the observation of operational radar, only double sending-double receiving scan pattern is carried out in operational dual polarization radar. Only four polarization parameters can be obtained by this pattern: differential reflectivity (Z_{DR}, unit: dB), differential propagation phase shift (Φ_{DP}, unit: °), specific differential propagation phase shift (K_{DP}, unit: °/km) and correlation coefficient (ρ_{HV}). The linear

depolarization ratio (L_{DR}, unit: dB) can only be obtained by the pattern of single sending-double receiving. Therefore, the direct RHI echoes and L_{DR} cannot be obtained for operational radars. In this study, NUIST CDP radar carried out the double sending-double receiving RHI scan pattern toward the strongest echo center of squall line (268° azimuth) at 23:25:41 on July 30, 2014 to obtain the high-resolution polarization data of the vertical structure of the squall line center. Then, the single sending-double receiving RHI scan pattern in this azimuth was carried out at 23:26:18, and the corresponding L_{DR} was obtained. These observation data are very rare.

2.2 Others weather data

The NCEP-NCAR reanalysis data used in this paper are from the NCEP/NCAR Reanalysis 1 Project of the National Oceanic and Atmospheric Administration (NOAA) in Boulder, Colorado, USA (Available at Physical Sciences Laboratory of NOAA website). The original daily grid data assimilated by this project are used, which cover a 2.5° × 2.5° global grid (144 × 73) and 17 pressure levels (1000, 925, 850, 700, 600, 500, 400, 300, 250, 200, 150, 70, 50, 30, 20, and 10 mb). The NCEP data documentation was separated into seven sections: Pressure Level, Surface, Surface Fluxes, Other Fluxes, Tropopause, Derived Data, and Spectral Coefficients. Each section contains a variety of data parameters.

In addition, the Micaps surface and high observation data and the automatic weather station data in NUIST provided by the NUIST meteorological station are also used in this study, including the conventional observation data of various meteorological stations in China, plotting data and other meteorological products. The automatic weather station is 1 km west of NUIST CDP radar. Sensors in this automatic station can automatically record temperature, pressure, wind, precipitation, radiation and other meteorological data. Figure 1 shows the location of the main meteorological observation stations in this study.

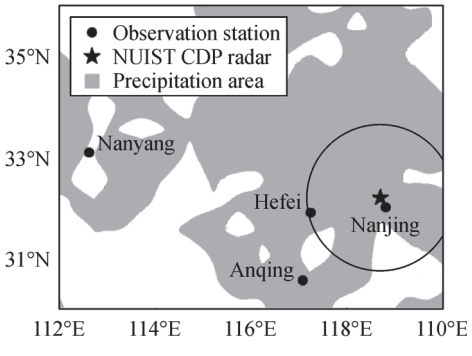

Fig. 1 The location of NUIST CDP radar and the main meteorological observation stations, and the influence range of squall line in this study. The circle represents the observation range of NUIST CDP radar.

2.3 Radar data quality control

When the electromagnetic wave of polarized radar passes through the rain area, the attenuations of Z_H and Z_V are different, which leads to the underestimation of Z_H and Z_{DR} at the rear side of precipitation. Therefore, attenuation correction must be carried out. Since Φ_{DP} is not affected by attenuation when the signal to noise ratio (SNR) is sufficient and its derivative K_{DP} has a linear relationship with rain intensity. The accuracy of the correction result is improved by the attenuation correction of K_{DP} (Bringi and Chandrasekar, 2001; Bukovcic et al., 2018). It is necessary to filter the ground clutter, determine the initial Φ_{DP} and smooth filtering before applying Φ_{DP} to K_{DP} calculation and attenuation correction.

In this paper, the quality control of Φ_{DP} data are carried out by the method of Φ_{DP} data classification and processing proposed by Du et al. (2012). The initial data bin is defined by 10 consecutive bins that set Φ_{DP} without abnormal fluctuation and $\rho_{HV} > 0.90$, and the average value of Φ_{DP} for these 10 bins is taken as the initial phase of the current radial. Finally, the preprocessed Φ_{DP} is obtained by sliding average filtering. Least squares fitting (LSF) is a common method to estimate K_{DP}, which can obtain accurate K_{DP} and avoid systematic deviation of accumulated rainfall. The fitting interval length is selected by the adaptive variable distance LSF method of Wang and Chandrasekar (2009). The fitted K_{DP} is used for attenuation correction.

Hu et al. (2008) considered that values of $K_{DP} < 0.1$°/km or $K_{DP} > 3.0$°/km are caused by observation error. To compensate for the error caused by observations, using the Z_H-K_{DP} combined method, the one-way attenuation rate of reflectivity (A_H, unit: dB/km) and the one-way attenuation rate of differential reflectivity (A_{DP}, unit: dB/km) is obtained as follows:

$$A_H = \begin{cases} \alpha K_{DP}, & 0.1 \leqslant K_{DP} \leqslant 3.0 \\ a Z_H^b, & K_{DP} < 0.1 \text{ or } K_{DP} > 3.0 \end{cases}, \quad (1)$$

$$A_{DP} = \begin{cases} \beta K_{DP}, & 0.1 \leqslant K_{DP} \leqslant 3.0 \\ c A_H^d, & K_{DP} < 0.1 \text{ or } K_{DP} > 3.0 \end{cases}, \quad (2)$$

where the parameters are $\alpha = 0.0987$ dB/°, $\beta = 0.0180$ dB/°, $a = 2.89 \times 10^{-5}$, $b = 0.77$, $c = 1.13$ and $d = 0.14$ (Huang et al., 2017; Islam et al., 2014; Ma, 2018). The corrected data are put into use for echo analysis in the following section.

2.4 Hydrometeor classification algorithm

The polarization parameters have obvious advantages in the characteristics analysis of the size, phase state, shape and orientation of the water condensate particles (Bringi and Chandrasekar, 2001). In this paper, hydrometeor classification algorithm (HCA) (Park et al., 2009) is

adopted to classify the hydrometeors. The radar parameters used are as follows: Z, Z_{DR}, ρ_{HV}, LK_{DP}, SD(Z) and SD (Φ_{DP}), where LK_{DP} is the logarithmic coordinate of K_{DP} as follows:

$$\begin{cases} LK_{DP} = 10\log K_{DP}, & K_{DP} > 10^{-3} \\ LK_{DP} = -30, & K_{DP} \leqslant 10^{-3} \end{cases}. \quad (3)$$

and the parameters SD(Z) and SD(Φ_{DP}) characterize the magnitude of the small-scale fluctuations of Z and Φ_{DP} along the radial. The estimates of SD(Z) and SD(Φ_{DP}) are obtained by averaging Z and Φ_{DP} data along the radial using a 1 km and 2 km running average window, respectively, subtracting the smoothed estimates from the original values, and calculating the root-mean-square (RMS) values of the residuals. The HCA identifies 10 classes of dual polarization radar echoes: 1) ground clutter, including that due to anomalous propagation (GC); 2) clear air, including turbulent and biological scatterers (CA); 3) dry aggregated snow (DS); 4) wet snow (WS); 5) crystals of various orientations (CR); 6) graupel (GR); 7) big drops (BD); 8) light and moderate rain (RA); 9) heavy rain (HR); and 10) a mixture of rain and hail (RH). The big-drops category designates rain with a drop size distribution skewed toward large raindrops. Big drop signatures are generally due to size sorting associated with convective updrafts often exemplified with Z_{DR} columns (Wakimoto and Bringi, 1988).

3 Weather analysis

3.1 Circulation background analysis

Figure 2 shows the weather charts at 08:00 on July 30, 2014, the trough at 200 hPa (figure omitted) is located from Hailar, Beijing, to northern Shandong. There is a −60°C cold center in eastern Baikal. The cold air flows southward under the guidance of strong north-west airflow behind the trough. There is a north jet to the north of the Northern China Plain at 300 hPa (figure omitted), which forms a deep trough in the Inner Monggolia Autonomous Region, Hebei, Henan and Hubei. There is a cut off vortex center near Beijing at 500 hPa. The vortex trough is located from Beijing to northern Hubei. The characteristics of longitudinal circulation behind the trough are obvious, which is conducive to the transport of cold advection. The subtropical high in the Western Pacific is rapidly uplifted to the north under the influence of severe tropical storm Nakri, and the Yangtze River basin is in the west and south-west airflow at the edge of the subtropical high. There is a cold vortex at 700 hPa near Hebei. The location of the trough is consistent with 500 hPa. The Yangtze and Huaihe River basins are affected by south-west warm and humid airflow. There is a small vortex between Xingtai and Jinan at 850 hPa, a trough and a warm shear line at the intersection of Hebei, Henan and Shandong. The warm and wet airflow in the middle and lower layers intersects around the Yangtze and Huaihe River basins. Convergence and uplift are conducive to the occurrence of strong convection.

At 20:00 on July 30, 2014 (Fig. 3), the trough at 200 hPa (figure omitted) was located from south of northeast China to Shandong Peninsula. North-west airflow after the trough is weakened. The temperature north of the middle and lower Yangtze River basin decreases, indicating that the high-level dry cold air intruded downward. The vortex located in Beijing moves eastward to the Liaodong Peninsula at 500 hPa. With the further development and deepening of the trough, the vortex extends from the Liaodong Peninsula to northern Hubei. Longitudinal circulation behind the trough strengthens, and the maximum speed of the north-east jet reaches 20 m/s, which is conducive to the transmission of cold air to the trough area. There is a south-west jet in front of the trough with similar intensity and intense wind shear in the trough area. The velocity of the trough slows due to the north-westward movement of typhoon No. 12, 2014. Cold centers are

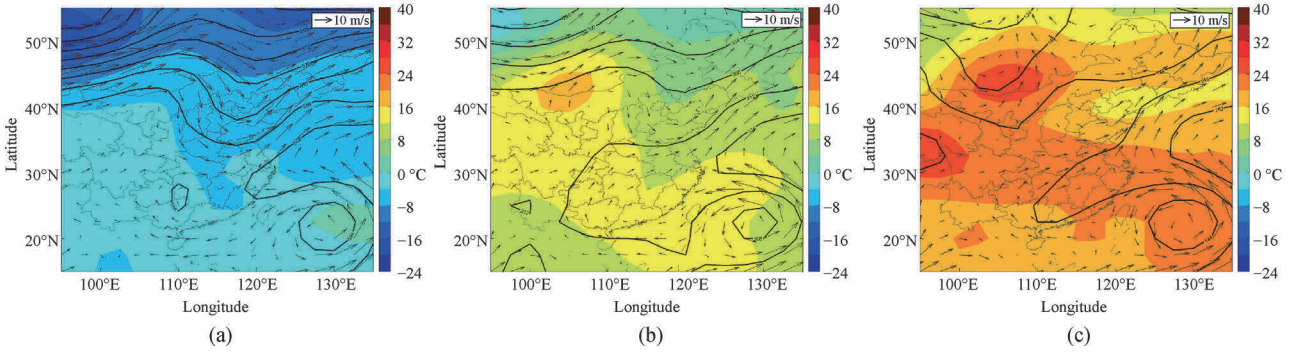

Fig. 2 Weather charts at 08:00 on July 30, 2014, (a) 500 hPa, (b) 700 hPa and (c) 850 hPa. The black line represents isobaric surface, the vector arrow represents wind, and the color represents temperature.

formed in the trough area, covering all of Shandong, most of Henan and Anhui, northern Jiangsu, eastern Hubei and northern Jiangxi, which are affected by the influence of the northern jet behind the trough. There is a narrow warm tongue in most of Zhejiang and southern Jiangsu. The position of the trough at 700 and 850 hPa is nearly motionless and coincides with the position at 500 hPa. The warm and humid airflow in the south-east of the tropical depression increases to approximately 10 m/s at 850 hPa, which provides abundant water vapor for the trough area and is conducive to the maintenance of strong convective weather and heavy rainfall.

3.2 Unstable conditions analysis

In weather analysis and forecast, the K index (K, unit: °C), Showalter index (SI, unit: °C) and convective available potential energy (CAPE, unit: J/kg) are commonly used to represent the stability of atmospheric stratification and convective energy (Cimini et al., 2015; Oliveira and Oyama, 2009). In general, the large K and negative SI represent the unstable atmospheric stratification. The large CAPE represents large convective energy. The sounding data before the formation of squall line is important to judge the unstable conditions and weather forecast. Figure 4 shows the *T*-log*P* plots of the three stations before the squall line is formed: the area of squall line formed (Nanyang), the area of squall line developed (Anqing) and the location of radar (Nanjing). According to the sounding data of Henan, Anhui and Jiangsu at 08:00 on July 30, the K is above 32°C, and its maximum value reaches 47°C. The SI of most stations is negative. The CAPE is generally greater than 1300 J/kg, and its extreme values are 3259 J/kg and 4278 J/kg, appearing in southern Jiangsu and Anhui, respectively.

The vertical structure of the atmosphere in the Yangtze and Huaihe River basin has shown the characteristics of strong convective weather. Taking Nanjing as an example, water vapor is abundant in the middle and lower troposphere, and the relative humidity (RH) below 600 hPa is larger than 74%. The south-east jet at 850 hPa makes the RH near the ground larger than 90%, and thus the water vapor is nearly saturated. A westerly exists in the upper layer, but an easterly appears in the lower layer. The vertical structure of the atmosphere presents the

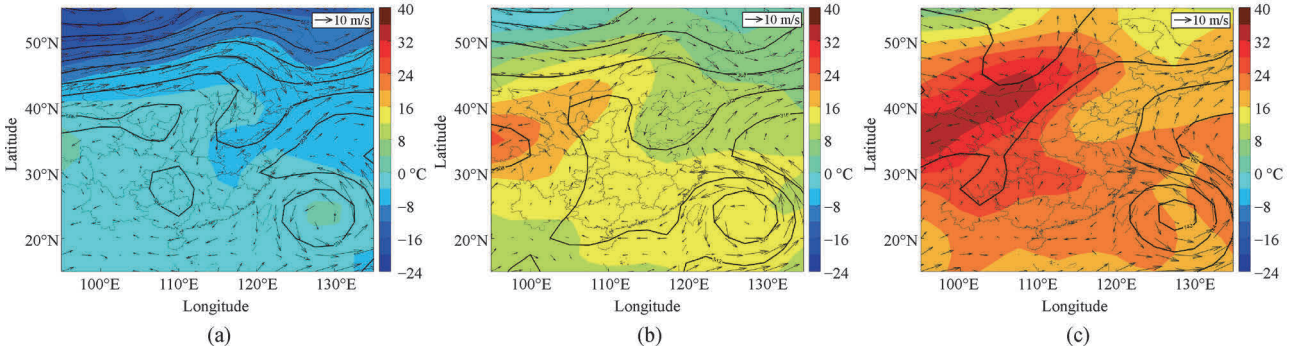

Fig. 3 Same as in Fig. 2 but at 20:00 on July 30, 2014.

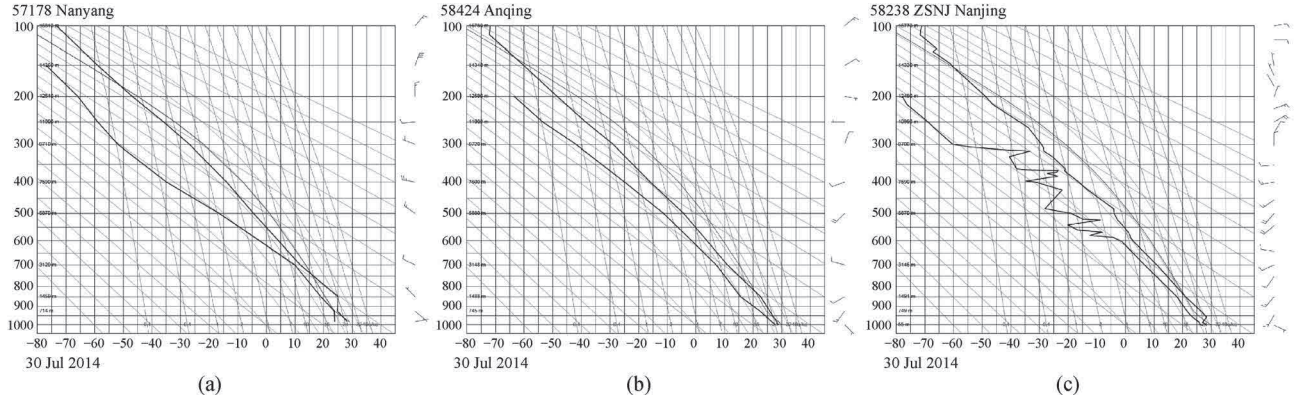

Fig. 4 *T*-log*P* plots at 08:00 on July 30, 2014; (a) Nanyang, (b) Anqing and (c) Nanjing.

characteristics of "clockwise rolling flow". It can be estimated that the thickness of warm clouds in Nanjing is close to 5 km from the lifting condensation level (LCL) and zero-degree layer height (ZH) in Table 2, which is beneficial to the development of strong convection. Besides, many studies have shown that the occurrence of hail does not require strong humidity condition (Gaviola and Fuertes, 2010; Zhang et al., 2013). The vertical structure of the "upper dry and lower wet" is favorable to the formation of hail, rather than the atmospheric structure with abundant water vapor (Huang et al., 2014; Levi et al., 1994). Therefore, the vertical structure in Nanjing is conducive to the formation of hail.

3.3 Actual weather analysis

The pressure, temperature, humidity and other meteorological elements change significantly when the squall line passes through, as shown in Fig. 5. Within 3 h, the pressure of Hefei rises by 4.2 hPa, the temperature decreases by 8°C and the temperature-dew point difference decreases from 6°C to 1°C. The 6-h precipitation at 02:00 on July 31, 2014 is 46 mm. The meteorological elements of Nanjing also change evidently. The squall line is in the dissipation stage when it passes through Nanjing, so the precipitation of Nanjing is not significant.

Data collected by the NUIST automated station provided a better view of the abrupt changes in meteorological elements as the squall line passed the radar station. It can be seen that there is a wind direction shear from east wind to west wind, and a wind speed shear from less than 1.0 m/s to more than 5.0 m/s at 00:40, indicating that the gust front is passing through at this time (Figs. 6(a) and 6(b)). The rainfall is not beginning, and the squall line does not arrive at the radar at this time. The centralized precipitation occurred around 01:40, indicating that the main body of

Table 2 Sounding data in Nanjing at 08:00 on July 30, 2014

	LCL	CCL	LFC	ZH	EL
P/hPa	987.5	917	871.5	560	147.5
H/m	171.3	826	1271.4	5144.7	14431.1
T/°C	27.1	25.5	22.5	0	−61.2
T_d/°C	26	21.6	19.2	-	-
q/(g·kg^{-1})	21.46	17.69	16.03	-	-
RH/%	94	79	82	-	-
e/hPa	35.9	32.63	27.23	6.11	0.01
θ/°C	28.19	32.98	34.34	49.27	93.32
θ_e/°C	90.79	85.43	82.09	-	-
θ_{se}/°C	95.19	99.82	93.09	71.14	93.90

Notes: LCL = lifting condensation level, CCL = convective condensation level, LFC = level of free convection, ZH = zero-degree layer height, EL = equilibrium level.

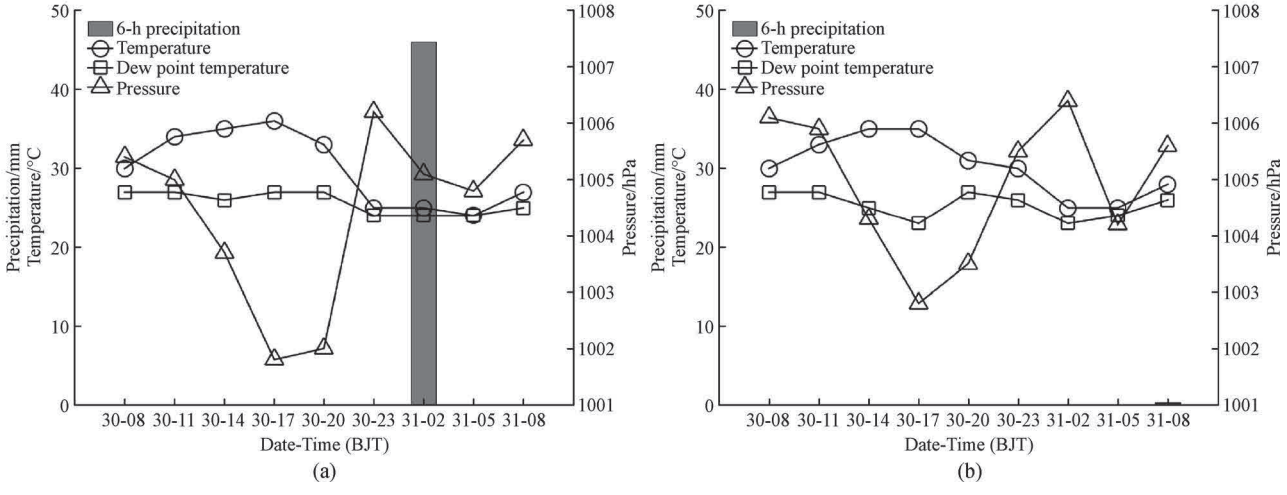

Fig. 5 Meteorological elements in (a) Hefei and (b) Nanjing.

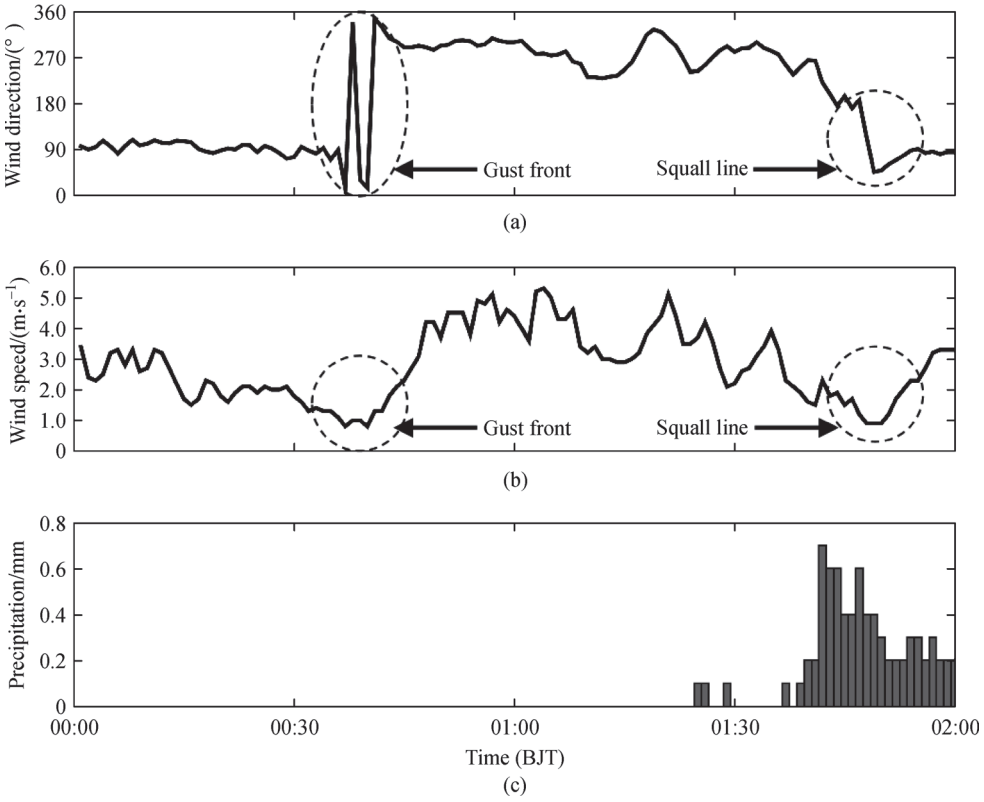

Fig. 6 (a) The average wind direction in 1 min, (b) the horizontal average wind speed in 1 min and (c) the precipitation per minute of automatic weather station in NUIST on July 31, 2014. The time of gust front and squall line passed through are circled.

the squall line passed the radar station at 01:40 (Fig. 6(c)). The weak wind under cloud (< 1.0 m/s) and wind shear are signals for the pass of the squall line at 01:40 (Figs. 6(a) and 6(b)), indicating the beginning of rainfall.

4 Results and discussion

4.1 Echo evolution

Figure 7 shows the squall line echoes. The main convective cloud is matured and locates 120 km west of the radar, and the maximum vertically integrated liquid (VIL) in this cloud is more than 65 kg/m^2 at 22:10 on July 30. The downdraft produced by heavy rainfall cut off the transport, lifting and condensing of warm moisture airflow to this cloud, gradually weakening the main convective cloud (figure omitted). In the south-east warm moisture area approximately 30 km in front of the main convective cloud, several smaller, newly scattered convection bubbles located at the red circle in Fig. 7(a) are triggered at the same time. The development speed of the new bubbles is extremely fast, and the echo intensity has exceeded 50 dBZ at 22:22, as shown in Fig. 7(a). The new cells are continuously generated west and south-west of the radar. The area north of the new cells gradually merges with the main convective cloud and continues to strengthen. An orderly array of strong convective cloud belts is formed, with a length of nearly 200 km, a width of only 10 km, and an echo center intensity of 55 dBZ at 22:57. The area before the squall line is controlled by the south-east warm and humid airflow from the Doppler radial velocity (V), which is conducive to the development of convection and precipitation. After the squall line, there is a strong westerly. Doppler radial velocity ambiguity appears, and there are many obvious mesocyclones in the system located at the red circle in Fig. 7(e). At 23:28, the supercell located at 230°−250°, 60−80 km is particularly significant, where Z and the echo top (ET) are above 55 dBZ and 14 km, respectively. There is a positive and negative velocity couple of 14 m/s in the center, in which the structure is symmetric and the velocity is equivalent. Rotation characteristics in this supercell are obvious. The squall line moved eastward over the radar and began to weaken at 01:38 on the 31st, July. The line breaks into a large area of flocculent echo with an intensity of 25−35 dBZ. The convection process tended to end when the whole atmosphere in Nanjing turned westerly. Figures 7(d) and 7(f) correspond to the weakening and dissipation of the squall line, respectively.

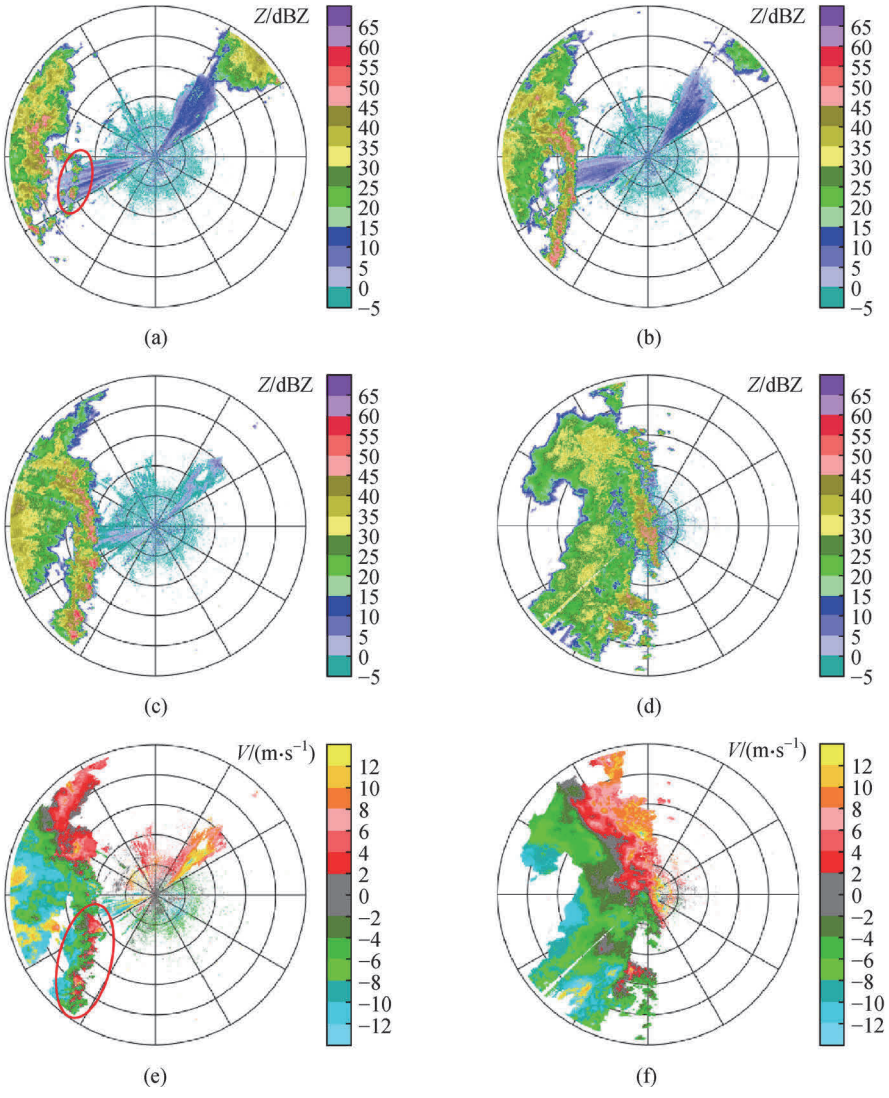

Fig. 7 Squall line echoes taken at 1.45° at (a) 22:22 *Z*, (b) 22:57 *Z*, (c) 23:28 *Z* and (e) 23:28 *V* on July 30, 2014, and (d) 01:38 *Z* and (f) 01:38 *V* on July 31, 2014. The distance circles represent 30 km. The red circles in (a) and (e) are the location of newly scattered convection bubbles and mesocyclones, respectively.

4.2 Polarization echo characteristics of the squall line

4.2.1 Horizontal structure

The polarization parameters have evident advantages in the characteristics analysis of the size, phase state, shape and orientation of the water condensate particles (Bringi and Chandrasekar, 2001). The large-scale liquid phase particles are affected by gravity, surface tension and air resistance in condensation and precipitation. The shape of these particles tends to be flat, approximately rotating oblate ellipsoid, and the degree of nonspherical is positively related to the particle scale (Zhang et al., 2001). Therefore, large rain drops can produce a large Z_{DR}. In addition, the melting hails can produce an outer ellipsoid water shell. C-band radar can also obtain a larger Z_{DR} when observing the convective precipitation center area (Fig. 8(b)) under the influence of the resonance effect of Mie scattering at the frequency of 5.5 GHz (C-band) (Rasmussen and Heymsfield, 1987; Meischner et al., 1991). Taking 23:28 on the 30th as an example, there are many strong echoes of 45–55 dBZ embedded in the clouds, and the corresponding Z_{DR} is 3.5–5.0 dB during the period of strong squall line development, reflecting that there are many large rain drops or wet hails in the cloud.

The different phase states of particles result in a certain phase difference in the horizontal and vertical polarization waves. Therefore, the fitted K_{DP} can also directly reflect the scale and deformation degree of particles in convective clouds. The K_{DP} is basically above 0.50°/km, and the

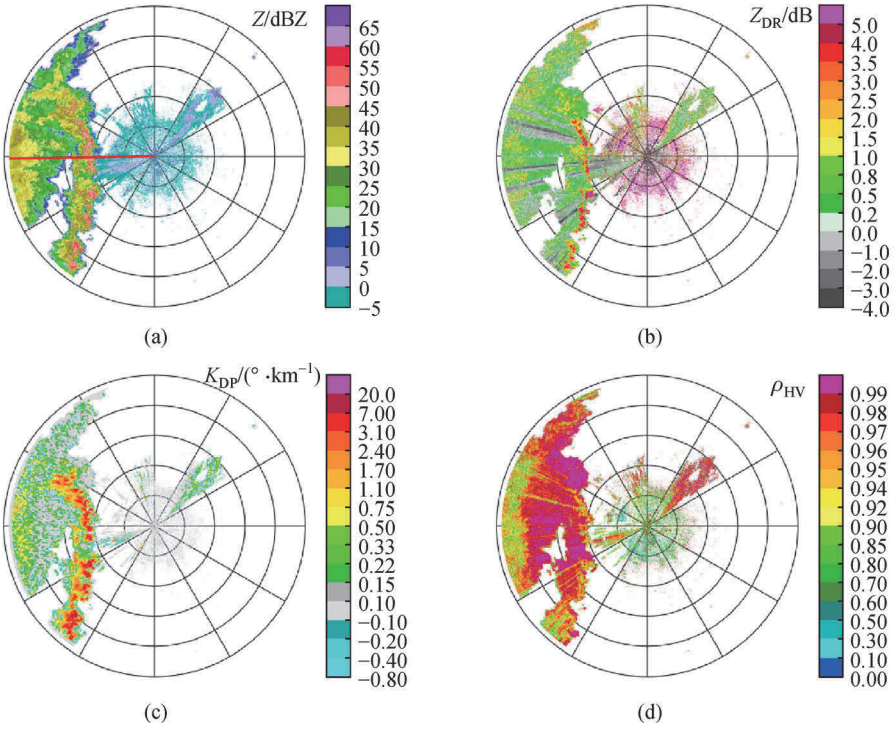

Fig. 8 Squall line echoes taken at 1.45° from (a) Z, (b) Z_{DR}, (c) K_{DP} and (d) ρ_{HV} at 23:28 on July 30, 2014. The distance circles represent 30 km. The red section line in (a) represents the location of the vertical cross section shown in Fig. 9 and Fig. 10.

strong echo is above 3.10°/km, as shown in Fig. 8(c). The nonspherical characteristics of particles are more obvious.

The horizontal and vertical polarization signals in the medium composed of the same particles have a strong and consistent correlation. The ρ_{HV} in the pure liquid phase particles is basically above 0.97, which is independent of the precipitation intensity. However, the ρ_{HV} in the area producing hails or melting hails can be reduced to below 0.95 (He et al., 2010). At the edge of the radar detection range of approximately 120–145 km, low values of approximately 0.90 appear in ρ_{HV}, as shown in Fig. 8(d). A strong echo at approximately 30−45 dBZ appears in Z. At the same time, the corresponding location in Z_{DR} and K_{DP} also appears to be a stronger echo than the surrounding area. Combined with the elevation, the altitude of this position is approximately 4 km. Sounding data in Nanjing at 20:00 on the 30th and 08:00 on the 31st show that the ZHs are 5.675 km and 5.0 km, respectively. It is determined to be the melting layer through the change in polarization parameters. Such echo characteristics appear in the transformation process from the ice phase to the liquid phase under the joint influence of melting, coalescence, velocity effect, particle shape, broken effect and other factors.

4.2.2 Vertical structure

To obtain the delicate vertical structure of convective clouds, RHI scan pattern is carried out at an azimuth of 268° (follow the red section line in Fig. 8(a)) at 23:25:41 and 23:26:18 on July 30, 2014 by double sending-double receiving and single sending-double receiving scan patterns, respectively. The conventional dual polarization parameters and L_{DR} parameter of 37 s time difference are obtained. To reflect the advantages of direct RHI scan pattern, a vertical cross section at the location of the red section line in Fig. 8(a) is obtained based on the VCP data, as shown in Fig. 9.

RHI scan pattern with a 0.54° beam width can obtain a more precise and delicate vertical structure compared with

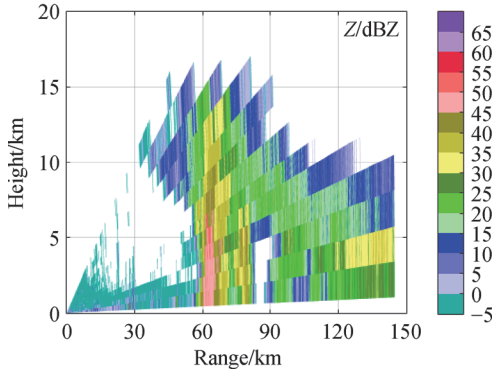

Fig. 9 The vertical cross section at 268° (follow the red section line in Fig. 8(a)) based on the VCP data at 23:28 on July 30, 2014.

RHI interpolation, as shown in Fig. 10. According to Figs. 9 and 10, the authenticity and resolution of patchwork RHI are obviously poorer than that of direct RHI scan pattern. In Fig. 10(a), a convective cell in the squall line is 60 km away from radar. The height of convection is more than 15 km, and the maximum Z in the echo core is more than 55 dBZ, which is located at a height of 3–7 km. The strong echo above 45 dBZ is over 10 km, and it has touched the ground. Typical supercell echo characteristics appear, such as echo wall, boundary weak echo range (BWER) and suspended echo. There is a convective cell behind the supercell, 80 km away from the radar, which also produces a relatively high Z and heavy precipitation. The 0°C bright band above 30 dBZ appears in the layered cloud echo above 120 km from the radar.

The updraft in front of the squall line runs through the whole supercell, which plays an important role in the development and maintenance of the squall line in V (Fig. 10(b)). BWER corresponds to the position of the updraft, and the suspended echo appears above the inflow. The divergence and outflow appear at the top of this cell, the Doppler radial velocity ambiguity appears, and vertical suction is obvious, which provides a stable vertical circulation for the development of strong convection. The back of this supercell is the downdraft. A positive and negative velocity shear corresponds to the echo core. This supercell has a typical airflow structure of a mature cell. The Doppler radial velocity ambiguity also appears in the 0°C bright band, which proves that the falling velocity increases after the raindrops melt.

Combined with the polarization parameters, the types of water condensate particles in the super cell can be distinguished accurately, as shown in Figs. 10(c) to 10(f). Before the formation of the squall line, the atmospheric vertical structure in Nanjing is characterized by “upper dry and lower wet”, strong wind shear at low level and large CAPE. These characteristics are conducive to the formation of hail, consistent with Zhang et al. (2013) and Huang

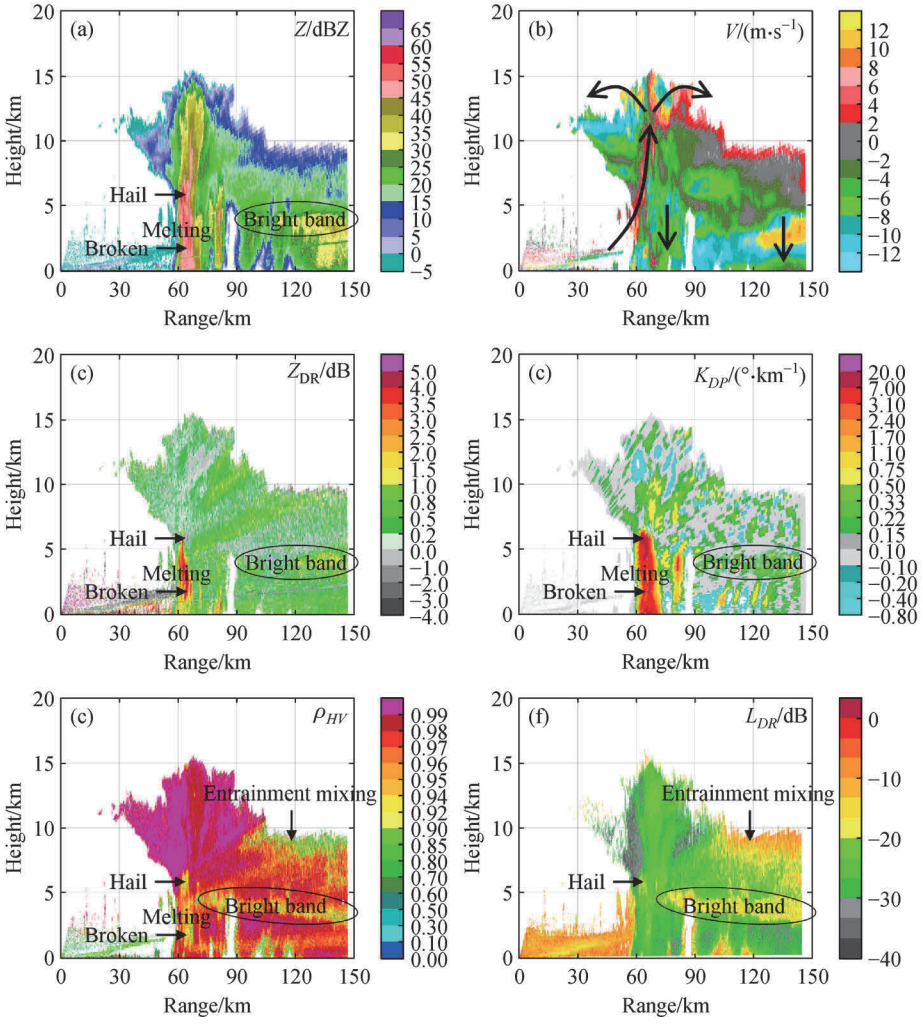

Fig. 10 RHI echoes of (a) Z, (b) V, (c) Z_{DR}, (d) K_{DP} and (e) ρ_{HV} at 23:25:41; (f) L_{DR} at 23:26:18 on July 30, 2014. The thick arrows in (b) represent airflow.

et al. (2014). Therefore, the echo core top corresponds to a Z_{DR} of not more than 0.5 dB, and Z_{DR} values less than 0 appear on the right side of the echo core top. Hails of more than −20 dB in L_{DR} appear on the echo core top, which is more obvious than that in Z_{DR}, and the hail ρ_{HV} is reduced to less than 0.90. The hails identified by HCA is located at the echo core top shown in Fig. 11.

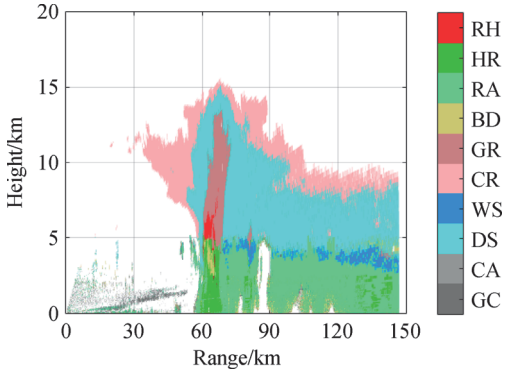

Fig. 11 Results of hydrometeor classification by HCA at 23:25:41 on July 30, 2014. The HCA classes are defined as (from bottom to top of color bar) GC = ground clutter, including that due to anomalous propagation, CA = clear air, including turbulent and biological scatterers, DS = dry aggregated snow, WS = wet snow, CR = crystals of various orientations, GR = graupel, BD = big drops, RA = light and moderate rain, HR = heavy rain, and RH = a mixture of rain and hail.

During the falling of hail, it melts to form an outer ellipsoid water shell, which leads to Z_{DR} values of approximately 3.5−4.0 dB and K_{DP} values of more than 3.10°/km in the middle and lower parts of the echo core. The Z_{DR} column is clearly visible in Fig. 10(c), and its ρ_{HV} is 0.90–0.95; even a few ρ_{HV} values of 0.85 appear. The existence of the Z_{DR} column indicates the positive temperature disturbance associated with the updraft (Illingworth et al., 1987; Pan et al., 2020). Big drop signatures in Fig. 11 are due to size sorting associated with convective updrafts exemplified with Z_{DR} columns (Wakimoto and Bringi, 1988). The vertical rising speed is weaker than that in the main updraft, which cannot hold the large raindrops and ice phase particles, such as graupel and hails, so they start to fall and drag the air to the downdraft. The ice phase particles melt during falling and grow after collision with the cloud droplets. Part of the particles re-enter into the upflow through the inflow, and the wet hail that is not completely melted will release latent heat of phase transition in the upflow, which will further promote the development of the upflow. These particles continue to grow in the updraft. When the particles grow to a certain extent, their falling velocity matches that of the updraft, and they will stay in the cloud, thus forming a top-down Z_{DR} large value region. This Z_{DR} growth mechanism is similar to the simulation results of Kumjian et al. (2014).

With the further melting and falling of precipitation particles, affected by gravity, particles continue to flatten, and the eccentricity of ellipsoids continues to increase until the surface tension of water causes large particles to break up into small particles, which corresponds to the largest Z_{DR} and the smallest ρ_{HV}, at a height of approximately 2.4 km. Hail melts completely at lower altitudes, with $\rho_{HV} > 0.98$.

The above phenomenon and discussion of polarization parameters are consistent with the results of Giangrande et al. (2008). In addition, the polarization parameters are more sensitive to the melting layer than Z. The Z_{DR}, K_{DP} and L_{DR} have obvious bright bands at heights of 3−5 km behind the supercell, especially for L_{DR}, and ρ_{HV} also has a significantly low value area. The hydrometeor type corresponding to bright bands is wet snow. The entrainment mixing process of ice crystals and air in the convective upper boundary at 9 km manifests as ρ_{HV} under 0.90 and L_{DR} of approximately −10 dB.

4.3 Polarization characteristics and echo formation mechanism of the gust front

A strong, cold downdraft usually exists in front of the squall line, expanding rapidly along the ground and forms a gust front when it meets the warm and humid airflow. The gust front can be seen in the radar echo. It is determined to be the atmospheric turbulence in the commonly used radar echo recognition and water condensate classification algorithms (Park et al., 2009; Straka et al., 2000). The reflectivity of turbulence (η) is given by Tatarski (1971) and Wilson et al. (1994):

$$\eta = 0.38\lambda^{-1/3} \cdot a^2 \Delta n^2 L_0^{4/3}, \tag{4}$$

where λ is the radar wavelength; a is the dimensionless constant; n is the atmospheric refractive index; and L_0 is the outer scale of turbulence. The atmospheric refractive index turbulence structure constant is represented by $a^2\Delta n^2 L_0^{4/3}$. According to Eq. (4), the echo intensity of turbulence is positively correlated with the outer scale of turbulence, so Z_{DR} can be used as a criterion for the difference between horizontal and vertical scales of turbulence.

Figure 12 shows the time series echoes of Z, V, Z_{DR} and ρ_{HV}, corresponding to three consecutive moments at 00:37, 00:44 and 00:51 on July 31, 2014. It is specifically stated that the colormap of Z_{DR} is changed to highlight the characteristics of the gust front. The squall line can be clearly confirmed by Z. The gust front is formed in the nonprecipitation area approximately 10−15 km in front of the squall line, which is slightly stronger than the surrounding echo (dotted line in Fig. 12). The gust front have reached the radar at the time around 00:40. The position of the gust front determined by radar echoes is

consistent with the observations obtained by the NUIST automatic weather station (Fig. 6). The gust front shows an obvious velocity convergence line in V, after which it is westerly. The ρ_{HV} of the gust front is stable at 0.70, which is different from other nonprecipitation clutters. The Z_{DR} of the gust front decreases first and then increases from north to south, and a negative Z_{DR} appears before and after the gust front. An important parameter that affects the shape of a fluid is its density. Turbulence is composed of air micromasses, and the density of turbulence is far less than that of precipitation particles. Therefore, when there is horizontal wind, the lateral shear stress on turbulence exerted by air will cause obvious deformation in the horizontal direction. In the gust front in the 330° direction, some abnormally high values with 8–9 dB of Z_{DR} appear, which are located in the red circle in Fig. 12(c). This phenomenon only occurs at lower elevations (below 3°), which is in line with the characteristics of the gust front echo. From the definition of Z_{DR} and Eq. (4), the ratio of horizontal and vertical scales of the turbulence is $L_H/L_V \approx$

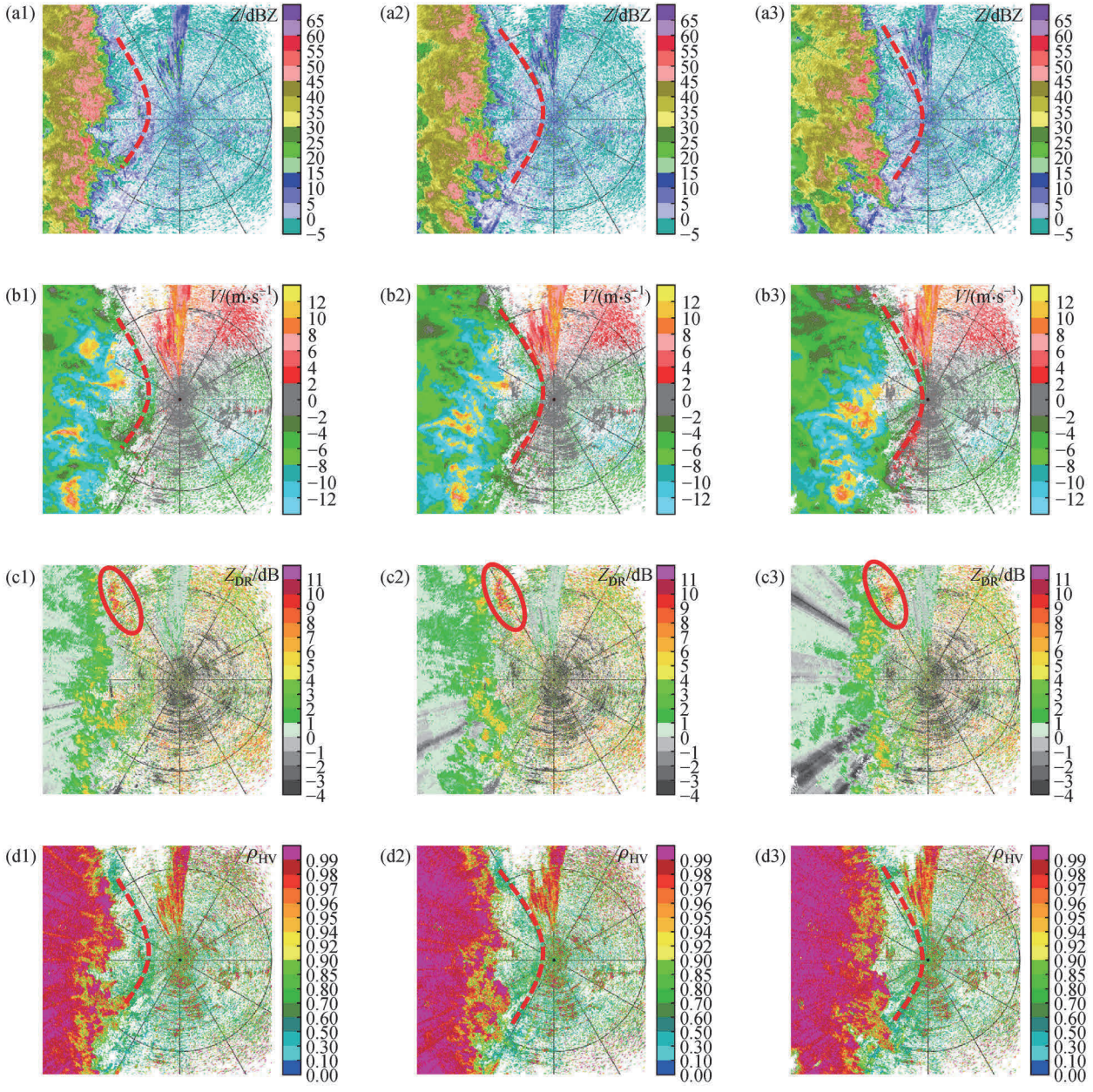

Fig. 12 Squall line echoes taken at 1.45° for (a) Z, (b) V, (c) Z_{DR} and (d) ρ_{HV} at 00:37, 00:44 and 00:51, respectively, on July 31, 2014. The distance circle and dotted line in (a), (b) and (d) represent 30 km and the location of gust front, respectively.

4.3. The turbulence is affected by strong westerlies in the gust front, which are arranged in a horizontal bar shape in the east–west direction. The long axes of the deforming turbulence in the 330° direction project completely on the radar cross section, which shows the maximum Z_{DR}. In contrast, it does not project at all in the 270° direction, so Z_{DR} decreases to 0. Meanwhile, warm air before the gust front is forced to rise, and the cold air after the gust front drops rapidly, which is different from the general horizontal moving atmosphere. In theory, it is speculated that the turbulence scale should be the maximum in the vertical direction, and the corresponding Z_{DR} in front and back of the gust front is negative, which is consistent with the observation. The observation confirms that the turbulence will be deformed by the influence of environmental airflow, forming a long ellipsoid turbulence in which the rotation axis and wind have the same direction. This finding is consistent with the discussion on the dual polarization parameters of the clear air echo by Huang et al. (2018). The scattering mechanism and the polarization characteristics of the turbulence echo can be further analyzed.

Take the westerly as an example shown in Fig. 13, which more vividly shows the reason that the Z_{DR} in the PPI map decreases first and then increases from north to south. Under the action of horizontal westerlies, the turbulence deforms into a long ellipsoid with an east–west direction rotation axis. When the radar is observed in the north or south direction, the horizontal scale of turbulence is the rotating axis α, and the vertical scale is the equatorial diameter (nonrotating axis β). The cross section of the turbulence detected by radar is an ellipse with a long axis and short axis of α and β, respectively. Currently, Z_{DR} is the maximum. When the radar is observed in the east or west direction, the horizontal and vertical scales of turbulence are all equatorial diameters (nonrotating axis β). The cross section of the turbulence detected by radar is a circle with diameter β; at this time, $Z_{DR} = 0$. When the radar is observed in other directions, the turbulence is not fully projected on the radar cross section, so the value of Z_{DR} is positive.

In Section 3.5 of part I, the formation mechanism and qualitative discussion of deforming turbulence echo are carried out. Quantitative discussion and parameterization of ZDR anomalies caused by the deforming clear air turbulence in front of the squall line will be discussed in part II.

5 Conclusions

1) The deep trough moves slowly under the obstruction of the tropical depression. The dry and cold air guided by the cold advection after the trough accumulates in the convection area, and the south-east jet around the severe tropical storm Nakri transports abundant water vapor for the trough area. The atmospheric instability is enhanced, and unstable energy is accumulated. The strong wind shear at low level prompted unstable energy released, which is important triggering mechanism for the squall line. The uniform spatial distribution of the trough area greatly strengthens the vertical gradient of pressure and the

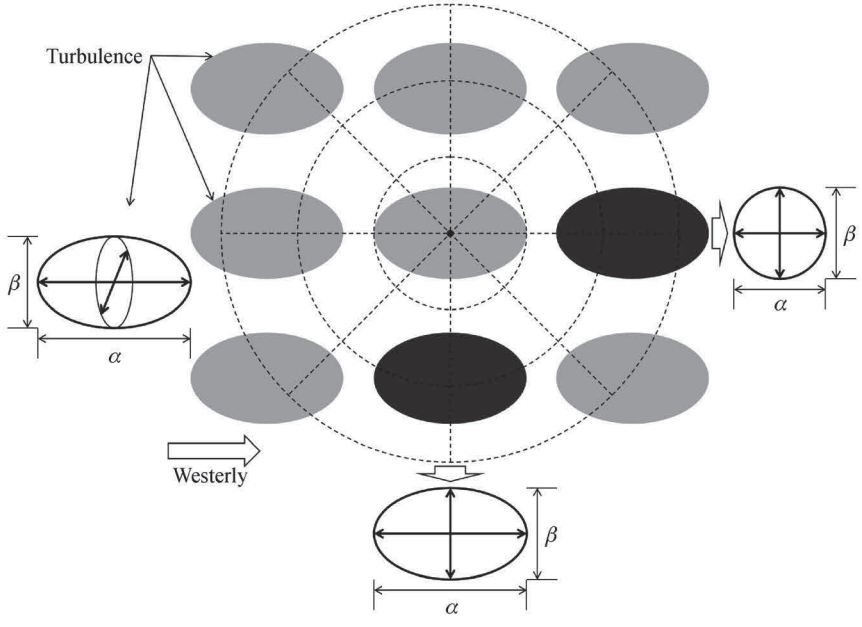

Fig. 13 Illustrating diagram of deforming turbulence echoes in the environmental westerly.

upward movement in front of the trough, which is conducive to the maintenance of strong convection and heavy precipitation. It provides favorable, large-scale environmental conditions for squall lines, and warm thick clouds are also conducive to the generation of high-efficiency precipitation.

2) The polarization parameters have obvious advantages in the characteristics analysis of the size, phase state, shape and orientation of the water condensate particles. RHI scan pattern can obtain more precise and delicate vertical structures of convective clouds. A convective cell in the squall line has typical supercell echo characteristics and a mature cell airflow structure. Through the comparison of the dual polarization parameters, the phase state of the water condensate particles in the supercell can be distinguished. There are small and medium raindrops, large raindrops, melting hail, dry hail and ice crystal particles in a supercell in the squall line, and the Z_{DR} column can be used to identify the location of the main updraft. In addition, the dual polarization parameters are more sensitive to the melting layer, especially for ρ_{HV} and L_{DR}.

3) The gust front is a narrow linear echo in Z that is affected by strong turbulence. It is an obvious velocity convergence line in V and approximately 0.70 in ρ_{HV}. The Z_{DR} can be used as a criterion for the difference between horizontal and vertical scales of turbulence. Turbulence, which is affected by environmental airflow, will cause an abnormally high Z_{DR} of 8−9 dB in the gust front and a negative Z_{DR} before and after the gust front. The change in Z_{DR} depends on the turbulence arrangement, orientation, and the relative position between turbulence and radar.

These characteristics of dual polarization parameters are helpful to understand the structure and evolution of the squall line.

Acknowledgements This work was supported by the National Natural Science Foundation of China (Grant No. 41675029), the Natural Science Foundation of Shandong Province (Nos. ZR2020MD052 and ZR2020MD053), and the Shanghai Aerospace Science and Technology Innovation Fund Project (No. SAST2019-097).

References

Bringi V N, Chandrasekar V (2001). Polarimetric Doppler Weather Radar: Principles and Applications. Cambridge: Cambridge University Press

Bukovcic P, Ryzhkov A V, Zrnić D, Zhang G (2018). Polarimetric radar relations for quantification of snow based on disdrometer data. J Appl Meteorol Climatol, 57(1): 103–120

Bluestein H B, French M M, Tanamachi R L, Frasier S, Hardwick K, Junyent F, Pazmany A L (2007). Close-range observations of tornadoes in supercells made with a dual-polarization, X-band, mobile Doppler radar. Mon Weather Rev, 135(4): 1522–1543

Cimini D, Nelson M, Guldner J, Ware R (2015). Forecast indices from a ground-based microwave radiometer for operational meteorology. Atmos Meas Tech, 8(1): 315–333

Du M, Liu L, Hu Z, Yu R (2012). Quality control of differential propagation phase shift for dual linear polarization radar. Journal of Applied Meteorological Science, 23(6): 710–720

Gallus W A Jr, Snook N A, Johnson E V (2008). Spring and summer severe weather reports over the midwest as a function of convective mode: a preliminary study. Weather Forecast, 23(1): 101–113

Gaviola E, Fuertes A F (2010). Hail formation, vertical currents, and icing of aircraft. J Atmos Sci, 4(4): 116–120

Geerts B (1998). Mesoscale convective systems in the southeast United States during 1994–95: a survey. Weather Forecast, 13(3): 860–869

Giangrande S E, Krause J M, Ryzhkov A V (2008). Automatic designation of the melting layer with a polarimetric prototype of the WSR-88D Radar. J Appl Meteorol Climatol, 47(5): 1354–1364

He Y, Xiao H, Lv D (2010). Analysis of hydrometeor distribution characteristics in stratiform clouds using polarization Radar. Chin J Atmos Sci, 34(1): 23–34

Houze R A Jr, Biggerstaff M I, Rutledge S A, Smull B F (1989). Interpretation of doppler weather radar display of midlatitude mesoscale convective systems. Bull Am Meteorol Soc, 70(6): 608–619

Hu Z, Liu L, Chu R, Jin R (2008). Comparison of different attenuation correction methods and their effects on estimated rainfall using X-band dual linear polarimetric radar. Acta Meteorol Sin, 66(2): 251–261

Huang H, Zhang G, Zhao K, Giangrande S (2017). A hybrid method to estimate specific differential phase and rainfall with linear programming and physics constraints. IEEE Trans Geosci Remote Sens, 55 (1): 96–111

Huang Q, Wei M, Hu H, Abro M I (2018). Analysis of atmospheric wind, temperature and humidity structure and dual-polarization radar parameters of clear air echo. Meteorological Monthly, 44(4): 526–537

Huang Z, Xu G, Wang X, Tang Y (2014). Analysis on two hailstorm events in Xianning based on observations of ground-based microwave radiometer. Meteorological Monthly, 40(2): 216–222

Illingworth A J, Goddard J W F, Cherry S M (1987). Polarization radar studies of precipitation development in convective storms. Q J R Meteorol Soc, 113(476): 469–489

Islam T, Rico-Ramirez M A, Han D, Srivastava P K (2014). Sensitivity associated with bright band/melting layer location on radar reflectivity correction for attenuation at C-band using differential propagation phase measurements. Atmos Res, 135–136(1): 143–158

Kumjian M R, Khain A P, Benmoshe N, Ilotoviz E, Ryzhkov A V, Phillips V T J (2014). The anatomy and physics of Z_{DR} columns: investigating a polarimetric radar signature with a spectral bin microphysical mode. J Appl Meteorol Climatol, 53(7): 1820–1843

Langston C, Zhang J, Howard K (2007). Four-dimensional dynamic radar mosaic. J Atmos Ocean Technol, 24(5): 776–790

Levi L, Lubart L, Lassig J (1994). Study of a convective storm series and of precipitated hail in south Argentina. Atmos Res, 33(1–4): 75–91

Ma L (2018). Data quality control for weather radar reflectivity ractor and its application in regional radar composite. Dissertation for Master's Degree. Nanjing: Nanjing University of Information

Science & Technology

Meischner P F, Bringi V N, Heimann D, Holler H (1991). A squall line in Southern Germany: kinematics and precipitation formation as deduced by advanced polarimetric and doppler radar measurements. Mon Weather Rev, 119(3): 678–701

Meng Z, Yan D, Zhang Y (2013). General features of squall lines in East China. Mon Weather Rev, 141(5): 1629–1647

Oliveira F P, Oyama M D (2009). Radiosounding-derived convective parameters for the alcantara launch center. J Aerosp Technol Manag, 1(2): 211–216

Pan J, Jiang L, Wei M, Luo C, Gao L, Zheng X, Peng J (2020). Analysis of a high precipitation supercell based on dual polarization radar observations. Acta Meteorol Sin, 78(1): 86–100

Park H S, Ryzhkov A V, Zrnic D S, Kim K (2009). The hydrometeor classification algorithm for the polarimetric WSR-88D: description and application to an MCS. Weather Forecast, 24(3): 730–748

Parker M D, Johnson R H (2000). Organizational modes of midlatitude mesoscale convective systems. Mon Weather Rev, 128(10): 3413–3436

Rasmussen R M, Heymsfield A J (1987). Melting and shedding of graupel and hail. Part I: model physics. J Atmos Sci, 44(19): 2754–2763

Romine G S, Burgess D W, Wilhelmson R B (2008). A dual-polarization-radar-based assessment of the 8 May 2003 Oklahoma City area tornadic supercell. Mon Weather Rev, 136(8): 2849–2870

Straka J M, Zrnic D S, Ryzhkov A V (2000). Bulk hydrometeor classification and quantification using polarimetric radar data: synthesis of relations. J Appl Meteorol, 39(8): 1341–1372

Tatarski V I (1971). The effects of the turbulent atmosphere on wave propagation. National Technical Information, TT-68–50464

Wakimoto R A, Bringi V N (1988). Dual-polarization observations of microbursts associated with intense convection: the 20 July storm during the MIST Project. Mon Weather Rev, 116(8): 1521–1539

Wang Y, Chandrasekar V (2009). Algorithm for estimation of the specific differential phase. J Atmos Ocean Technol, 26(12): 2565–2578

Wilson J W, Weckwerth T M, Vivekanandan J, Wakimoto R M, Russell R W (1994). Boundary layer clear-air radar echoes: origin of echoes and accuracy of derived winds. J Atmos Ocean Technol, 11(5): 1184–1206

Zhang G, Vivekanandan J, Brandes E (2001). A method for estimating rain rate and drop size distribution from polarimetric radar measurements. Geoscience & Remote Sensing IEEE Transactions on, 39(4): 830–841

Zhang L, Guo R, He N, Liao X (2013). Characteristic analusis of a hail event in Beijing. Meteorol Sci Technol, 41(1): 114–120